

An enhanced MXene/LIG composite structure-based flexible sensor for real-time pilot motion monitoring

Mian Zhong(钟勉), Hongyun Fan(范红云), Zhanghui Wu(吴章辉), Xiaoqing Xing(邢晓晴), Yilin Zhao(赵一霖), Lin Li(李麟), Yong Jiang(蒋勇), Qinglei Li(李庆磊), Kaixin Xu(徐开心), Kun Luo(罗鲲), Guogang Ren(任国刚), and Jie Wu(吴杰)

Citation: Chin. Phys. B, 2026, 35 (**5**): 058102. DOI: 10.1088/1674-1056/ae32fe
http://cpb.iphy.ac.cn; http://iopscience.iop.org/cpb

What follows is a list of articles you may be interested in

Improving physical properties of poly(vinyl alcohol)/montmorillonite nanocomposite hydrogels via the Hofmeister effect

Rongrong Guo(郭蓉蓉), Deshuai Yu(余德帅), Yifan Huang(黄一帆), Sen Wang(王森), Cong Fu(付聪), Shuihong Zhu(朱水洪), Jia Yi(易佳), Hanqi Wang(王涵淇), and Youhui Lin(林友辉)
Chin. Phys. B, 2023, 32 (**8**): 088103. DOI: 10.1088/1674-1056/acdfc2

Enrichment of microplastic pollution by micro-nanobubbles

Jing Wang(王菁), Zihan Wang(王子菡), Fangyuan Pei(裴芳源), and Xingya Wang(王兴亚)
Chin. Phys. B, 2022, 31 (**11**): 118104. DOI: 10.1088/1674-1056/ac6161

Morphological modifications of C_{60} crystal rods under hydrothermal conditions

Ming-Run Du(杜明润), Shi-Xin Liu(刘士鑫), Jia-Jun Dong(董家君), Ze-Peng Li(李泽朋), Ming-Chao Wang (王明超), Tong Wei(魏通), Qing-Jun Zhou(周青军), Xiong Yang(杨雄), and Peng-fei Shen(申鹏飞)
Chin. Phys. B, 2020, 29 (**12**): 128102. DOI: 10.1088/1674-1056/abc0d8

Modulation of magnetic and electrical properties of bilayer graphene quantum dots using rotational stacking faults

Hong-Ping Yang(杨宏平), Wen-Juan Yuan(原文娟), Jun Luo(罗俊), Jing Zhu(朱静)
Chin. Phys. B, 2019, 28 (**7**): 078106. DOI: 10.1088/1674-1056/28/7/078106

Path integral Monte Carlo study of $(H_2)_n@C_{70}$ (n=1,2,3)

Hao Yan (郝妍), Zhang Hong (张红), Cheng Xin-Lu (程新路)
Chin. Phys. B, 2015, 24 (**8**): 088103. DOI: 10.1088/1674-1056/24/8/088103

An enhanced MXene/LIG composite structure-based flexible sensor for real-time pilot motion monitoring

Mian Zhong(钟勉)[1,†,‡], Hongyun Fan(范红云)[1,†], Zhanghui Wu(吴章辉)[1], Xiaoqing Xing(邢晓晴)[1], Yilin Zhao(赵一霖)[2], Lin Li(李麟)[3], Yong Jiang(蒋勇)[3], Qinglei Li(李庆磊)[4], Kaixin Xu(徐开心)[4], Kun Luo(罗鲲)[5], Guogang Ren(任国刚)[6], and Jie Wu(吴杰)[4,§]

[1] *College of Aviation Electronic and Electrical Engineering, Civil Aviation Flight University of China, Deyang* 618307, *China*
[2] *School of Mechanical Engineering and Mechanics, Ningbo University, Ningbo* 315211, *China*
[3] *School of Mathematics and Physics, Southwest University of Science and Technology, Mianyang* 621010, *China*
[4] *College of Art and Physical Education, Kyungil University,* 50, *Gamasil-gil, Hayang-eup, Gyeongsan-si, Gyeongbuk-do, Korea*
[5] *School of Materials Science and Engineering, Changzhou University, Changzhou* 213164, *China*
[6] *School of Physics, Engineering and Computer Science, University of Hertfordshire, Hatfield, Hertfordshire AL*10 9*AB, UK*

(Received 27 September 2025; revised manuscript received 10 December 2025; accepted manuscript online 4 January 2026)

Flexible sensors have emerged as a promising tool in applications ranging from pilot physiological monitoring to motion capture and complex training environments. However, conventional approaches often face inherent limitations, such as susceptibility to electromagnetic interference, instability in humid or sweat-rich conditions, and restricted multifunctional integration. To overcome these challenges, we present a flexible sensor based on a multifunctional MXene/LIG composite structure. By combining surface-modified MXene with laser-induced graphene (LIG), we developed a robust conductive framework characterized by hierarchical porosity. Thanks to this innovative design, the sensor achieves exceptional multifunctional performance. It exhibits high electromagnetic shielding effectiveness of 31.5 dB through synergistic reflection and absorption, demonstrates strong hydrophobicity with a contact angle of 151.1°, and delivers enhanced thermal conductivity. These features enable accurate monitoring of operational movements in simulated cockpit environments while ensuring durable performance under complex aviation requirements. Moreover, this design strategy offers a novel pathway for advancing high-performance flexible sensors, opening new opportunities in wearable electronics, healthcare monitoring, and intelligent human-machine interaction systems.

Keywords: laser-induced graphene (LIG), MXene, electromagnetic shielding, hydrophobicity, flexible sensor
PACS: 81.05.ub, 68.35.Ct, 72.80.Tm, 07.07.Df
DOI: 10.1088/1674-1056/ae32fe **CSTR:** 32038.14.CPB.ae32fe

1. Introduction

With the rapid advancement of flexible electronics and wearable technologies, there is a growing demand for high-performance and multifunctional sensors capable of reliable operation in complex environments.[1–3] Such sensors are expected to deliver excellent sensing performance while maintaining long-term stability,[4,5] even under conditions involving high humidity, sweat, or strong electromagnetic interference.[6,7] This requirement is particularly critical in fields such as aerospace, healthcare, and intelligent manufacturing, where sensors must integrate functions such as motion detection, environmental adaptability, and electromagnetic compatibility.[8–10] However, conventional sensors often face inherent limitations in these challenging environments, including limited resistance to electromagnetic interference, poor stability in humid or sweat-rich conditions, and restricted multifunctional integration.[11,12] These bottlenecks severely hinder their widespread application in demanding scenarios.

Laser-induced graphene (LIG) has emerged as a promising candidate for flexible electronic devices due to its simplified preparation process, high patterning precision, cost-effectiveness, and scalability.[13–15] Despite its advantages, pure LIG-based sensors typically suffer from limited electromagnetic shielding effectiveness and insufficient environmental adaptability, which hinder their application in multifunctional integration. In contrast, MXene materials offer high electrical conductivity, outstanding electromagnetic shielding performance, and good sensing capabilities.[16–20] The combination of MXene with LIG therefore provides a promising pathway to synergistically enhance conductivity, shielding, and sensing functionalities. Nevertheless, pristine MXene suffers from intrinsic hydrophilicity and susceptibility to oxidation, which severely compromise its long-term stability and environmental adaptability.[21–23] Although strategies such as surface functionalization and hybridization with polymers or carbon-based materials have been proposed to mitigate these issues, they often come at the expense of electrical conductiv-

[†]These authors contributed to this work equally.
[‡]Corresponding author. E-mail: mianzhong@cafuc.edu.cn
[§]Corresponding author. E-mail: wu3732596zh@163.com
© 2026 Chinese Physical Society and IOP Publishing Ltd. All rights, including for text and data mining, AI training, and similar technologies, are reserved.

ity and structural integrity. Thus, achieving an optimal balance between sensing performance, shielding effectiveness, and environmental stability remains a key challenge.

To address these challenges, this study proposes a novel modified MXene/LIG(M-MXene) composite sensor with exceptional electromagnetic shielding, hydrophobicity, and thermal conductivity, The sensor was fabricated by integrating surface-functionalized MXene with CO_2-laser-induced graphene on PI films, yielding a multifunctional composite that demonstrates robust performance in complex environments. Specifically, the material achieves high electromagnetic shielding effectiveness (31.5 dB) through synergistic reflection and absorption, exhibits strong hydrophobicity with a contact angle of 151.1°, and delivers enhanced thermal conductivity, ensuring reliable operation under simulated cockpit conditions. These advanced functionalities not only enable precise capture of pilots' movements but also highlight the sensor's potential to provide multidimensional support for enhancing flight safety. This design strategy offers promising insights for the development of high-performance flexible sensors with broad applications in wearable electronics, healthcare monitoring, and intelligent human-machine interaction systems.

2. Experimental details

2.1. Preparation of MXene/LIG composite film

Figure 1 illustrates the fabrication process of the MXene/LIG composite film. Initially, the preparation method for the MXene/LIG film was consistent with the steps reported in our previous work,[5] which involved immersing a PI film in an aqueous MXene dispersion, followed by drying and direct laser writing with a CO_2 laser to form the graphene layer. For the M-MXene/LIG composite film used in this study, we further employed CPTMS and FOTS as silane coupling agents to functionalize the surface of MXene, aiming to improve the interfacial compatibility and hydrophobicity. To prepare surface-functionalized MXene (FoShan XinXi Technology Co., Ltd., Foshan, CHN. Purity $\geq$ 98%), 400 g of finely ground $Ti_3C_2T_x$ powder was dispersed in a mixture of 3-Chloropropyltrimethoxysilane (CPTMS. Shanghai Aladdin Biochemical Technology Co., Ltd., Shanghai, CHN. Purity $\geq$ 97%) and Perfluorooctyltrichlorosilane (FOTS. Shanghai Aladdin Biochemical Technology Co., Ltd., Shanghai, CHN. Purity $\geq$ 97%) precursors (5% concentration in 40-mL ethanol) for 24 hours. The mass ratio of CPTMS to FOTS is set at 1:1. CPTMS and FOTS were selected as silane coupling agents; in particular, FOTS was chosen due to its fluorine-containing molecular chain, which is highly effective in imparting hydrophobic properties, while CPTMS facilitates general surface functionalization and is capable of forming cross-linking structures. After the reaction, the resulting suspension was purified by centrifugation using a deionized water and ethanol solution to remove unreacted silane molecules, ensuring a clean and effectively functionalized MXene surface. Subsequently, 20 mL of ethanol was carefully added to the top of the suspension, followed by complete drying under ambient conditions. To fabricate the M-MXene/LIG composite film, a 125-μm thick PI film (Shenzhen Jihongda Plastic Products Co., Ltd., Shenzhen, CHN) was pretreated by immersion in the as-prepared M-MXene dispersion prior to undergoing the LIG process, as shown in Fig. 1.

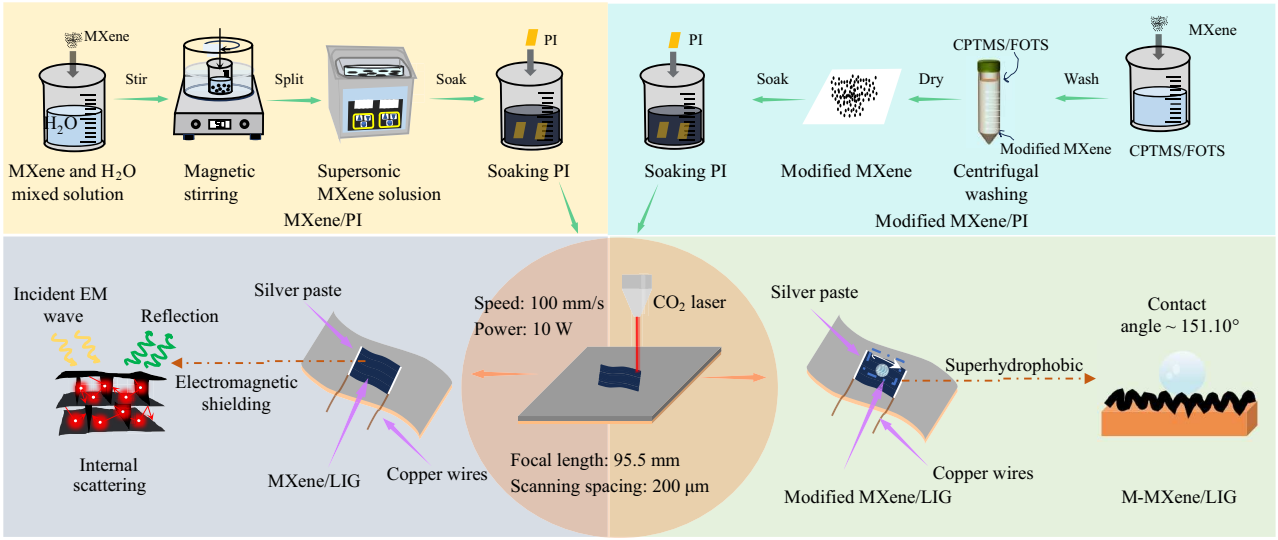


Fig. 1. Preparation, working principle, and application of M-MXene/LIG composite thin films.

First, the PI film was ultrasonically cleaned in deionized water for 10 minutes and then dried in an electric thermostatic drying oven (DHG-202, Shaoxing Subo Instrument Co., Ltd., Zhejiang, CHN) at 50 °C for 30 minutes. Subsequently, an M-MXene solution with a concentration of 20 mg/ml was prepared by accurately weighing a specific quantity of MXene powder and mixing it with deionized water in a beaker according to the predetermined ratio. The mixture was then thor-

oughly stirred using a magnetic stirrer. Due to the incomplete dispersion of MXene powder in deionized water, the mixture underwent further ultrasonication to obtain a well-dispersed M-MXene solution. The pretreated PI film was immersed in the prepared MXene solution for 30 minutes, followed by drying in a drying oven. This immersion-drying process was repeated 3 times to produce the dark-colored PI film coated with an MXene layer, as shown in the right side of Fig. 1. The repeated immersion of the PI film into the M-MXene solution, followed by drying, enabled the gradual and controlled adhesion of the M-MXene flakes onto the surface of the PI film surface. In the following sections, the LIG generated from the M-MXene/PI will be referred to as M-MXene/LIG and abbreviated as M-MXene/LIG. The PI film, now coated with the M-MXene layer, was mounted on a three-dimensional movable platform. A laser treatment was then conducted using a CO_2 infrared laser (Synrad P150, Novanta Corporation, Bedford, MA, USA) under fixed laser parameters: a focal length of 95.5 mm, laser power of 10 W, scanning speed of 100 mm/s, and scanning pitch of 200 μm. This process illustrates the corresponding relationship between the fabrication routes of MXene/LIG and M-MXene/LIG. The two processes are essentially identical, differing only in the surface modification step of MXene.

2.2. Material characterization

In this experiment, a scanning electron microscope (SEM; Thermo Scientific Helios 5 CX, Thermo Fisher Scientific Inc., Waltham, MA, USA) was employed to observe the microstructural morphology of the LIG surface. An energy-dispersive x-ray spectrometer (EDS; Thermo Scientific Helios 5 CX, Thermo Fisher Scientific Inc., Waltham, MA, USA) was used to analyze the elemental composition and distribution within the LIG. X-ray diffraction (XRD; Rigaku Ultima IV, Rigaku Corporation, Akishima, Japan) was conducted to identify the crystalline structure and corresponding peak intensities of the LIG. A Renishaw in Via confocal micro-Raman spectrometer (Raman, Gloucestershire, UK) was applied to determine the positions and intensities of the D, G, and two-dimensional (2D) Raman peaks of the LIG. X-ray photoelectron spectroscopy (XPS; FEI ESCALAB Xi+, Thermo Fisher Scientific Inc., Waltham, MA, USA) was performed to investigate the atomic species and their relative concentrations in the LIG. A microwave network analyzer (MNA; Agilent E5071C, Keysight Technologies Inc., Santa Rosa, CA, USA) was used to test the electromagnetic shielding performance of LIG. A digital multimeter (RIGOL DM3058E, RIGOL Technologies Co., Ltd., Suzhou, CHN) was employed for real-time resistance measurements, and a tensile testing machine (WNMC, Beijing, CHN) was used to assess the tensile strain properties of the material.

3. Results and discussion

3.1. Optical spectrum analysis

In this section, optical spectrum detection and analysis were performed on MXene/LIG samples fabricated via laser direct writing technology following the immersion of the PI film in an M-MXene solution. Figures 2(a)–2(c) show the SEM images of LIG, MXene/LIG, and M-MXene/LIG, which were used to examine the microstructural morphology of the graphene surface. Specifically, figure 2(a) displays the SEM image of LIG. As shown in Fig. 2(a), the PI film undergoes carbonization under laser irradiation, resulting in the formation of a porous carbon layer characterized by distinct strip-like textures aligned with the scanning path. This indicates the successful transformation of PI into a porous carbon structure containing graphene sheet. Figure 2(a1) further shows a more evident porous structure, with visible interlayer gaps and exfoliation features, forming a loosely packed structure with varying pore sizes that exhibit a "capillary channel" morphology. This unique structure provides potential "anchoring points" for subsequent MXene attachment and may contribute to enhanced sensing performance. However, the exposed nature of this structure renders it vulnerable to moisture and electromagnetic interference, which may compromise its long-term stability. Figure 2(a2) clearly displays a porous network structure, in which honeycomb-like pores are interspersed. The graphene flakes are loosely arranged with occasional stacking, showing a "flower-like" morphology, which facilitates charge transport and improves sensitivity. Figure 2(a3) reveals sharp edges of graphene, accompanied by curling and fragmentation; the porous channels remain at the nanoscale, contributing to the formation of an efficient responsive structure. This is a typical characteristic of laser-induced porous graphene, which is known for its electrical conductivity, gas permeability, and rapid response capability.

Figure 2(b) presents a magnified SEM image of MXene/LIG. In Fig. 2(b), the overall surface morphology appears rougher and more "fuzzy" or "fluffy" compared to Fig. 1(a), indicating that MXene has been embedded and partially integrated with the LIG surface. However, the attachment is uneven, with visible aggregation and localized surface protrusions. As shown in Fig. 2(b1), MXene flakes are observed stacking on the surface, with cracks still present between the flakes and the LIG substrate, indicating weak interfacial bonding and partial coverage of the graphene framework. Figure 2(b2) shows a more compact layered morphology. However, certain regions exhibit expanded and detached layers, indicating insufficient interlayer bonding, which leads to the formation of non-uniform conductive pathways. Additionally, the porous structure is partially filled, resulting in reduced gas permeability. In Fig. 2(b3), the surface roughness is further

increased, with MXene flakes exhibiting irregular coverage. Some flakes exhibit curled edges and surface cracks, indicating that they have not yet been stably anchored onto the substrate.

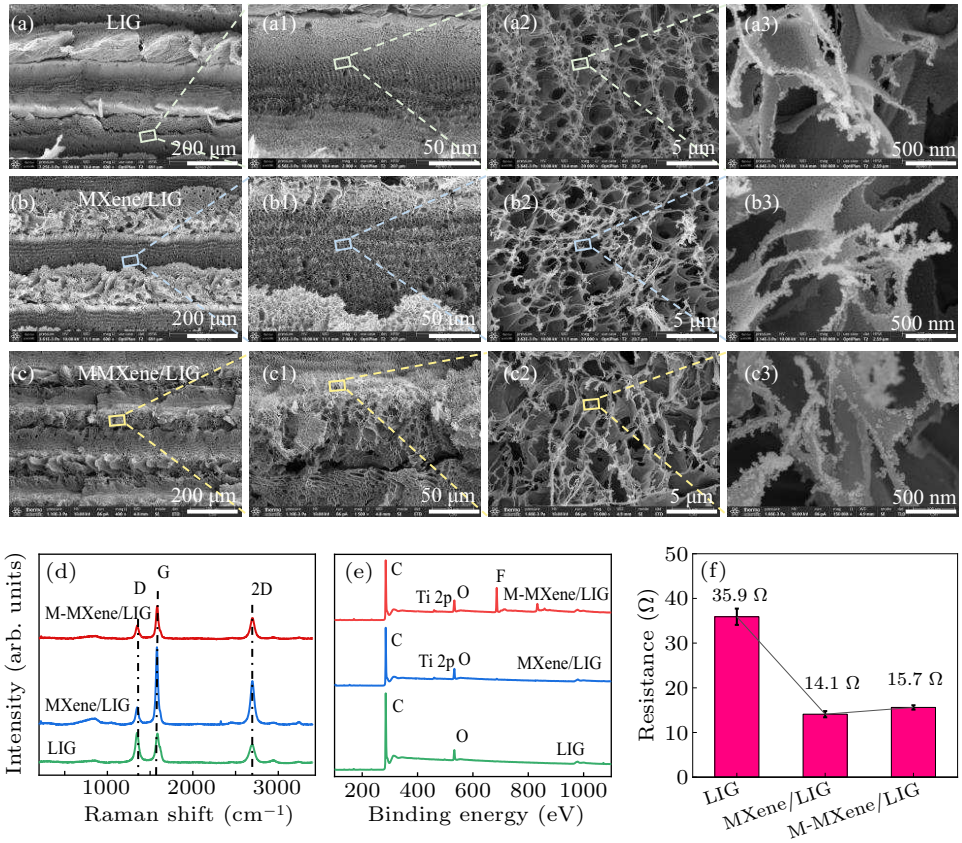


Fig. 2. Characterization of LIG, MXene/LIG, and M-MXene/LIG: (a) SEM image of LIG, (b) MXene/LIG composite, (c) M-MXene/LIG composite, (d) Raman spectroscopy analysis, (e) XPS analysis, (f) measurement of resistance values.

Figure 2(c) shows the SEM image of the M-MXene/LIG composite. As shown in Fig. 2(c), the surface morphology becomes more uniform without obvious aggregation, indicating that the M-MXene is more evenly distributed on the LIG surface, with sharper edges and improved compactness and structural stability. These characteristics contribute to enhanced resistance against moisture erosion and an extended service life. Figure 2(c1) clearly illustrates the integration of LIG flakes with MXene, presenting a "flat-rough-flat" gradient structure, which suggests the formation of a denser interfacial layer with strong adhesion between the modified materials. In Fig. 2(c2), the surface appears rough yet compact, without significant detachment observed, indicating the effectiveness of the modification process. This also indicates that the M-MXene exhibits improved dispersibility and adhesion, providing a solid structural foundation for subsequent stable performance. Figure 2(c3) demonstrates the absence of visible cracks or particle detachment, with layers more tightly connected and partially sealed pores. The hydrophobic layer may have formed a nanofilm-like coverage, further enhancing corrosion resistance. In summary, the three sets of SEM images shown in Figs. 2(a)–2(c) reflect the progressive evolution of the material from no additives, to the introduction of MXene, and finally to the use of M-MXene. Figure 2(a) corresponds to the basic porous graphene structure formed after the laser-induced carbonization of a pure PI film. Figure 2(b) displays the MXene/LIG composite, where the graphene pores formed under laser action are more uniformly distributed and the structure is more regular. In Fig. 2(c), the surface of the M-MXene/LIG exhibits more pronounced sheet stacking and coverage, indicating that the M-MXene is more likely to form a covering layer on the surface of the composite structure. The structural differences among the three present a progressive change from "LIG → MXene/LIG → M-MXene/LIG", which provides a morphological basis for the subsequent performance differences. EDS detection was performed on the M-MXene/LIG composite (Fig. S1(a) in supporting materials). Elemental spectral analysis revealed the presence of titanium (Ti) and fluorine (F) elements, confirming the incorporation of M-MXene within the LIG structure. Based on these observations, it can be inferred that the M-MXene/LIG composite utilized in this experimental set may exhibit enhanced hydrophobic properties.

Subsequently, Raman and XPS analyses were performed on LIG, MXene/LIG, and M-MXene/LIG, with the results shown in Figs. 2(d)–2(e). Figure 2(d) demonstrates the offset-stacked Raman spectra of LIG, MXene/LIG, and M-MXene/LIG. The D peak observed at 1350.108 cm^{-1} is in-

dicative of sp^3-hybridized carbon atoms and structural defects. The G peak at 1582.489 cm^{-1} corresponds to sp^3-hybridized carbon atoms and reflects the graphite crystal structure. The 2D peak at 2697.143 cm^{-1}, represents the second-order harmonic of the G peak and is closely associated with the number of layers and the degree of crystal order. The I_D/I_G and I_{2D}/I_G ratios exhibit distinct trends, which are closely associated with the extent of graphene defects, the crystalline structure of graphene, and the variations in the number of graphene layers. In LIG, the I_D/I_G ratio is relatively higher at 1.026, indicating a greater density of defects. Meanwhile, the I_{2D}/I_G ratio of 0.620 indicates a larger number of graphene layers and a moderate degree of structural order. This phenomenon may be attributed to the formation mechanism of LIG via laser ablation of polyimide, which typically results in a higher concentration of edge defects and regions with non-ideal graphite crystallinity. Consequently, the D peak is more pronounced, reflecting a higher level of defects and a generally developed graphitic structure. In MXene/LIG composites, the I_D/I_G ratio is 0.213, which represents a significant decrease compared to that of pure LIG, indicating a considerable reduction in defects density. Meanwhile, the I_{2D}/I_G ratio is slightly lower at 0.555, suggesting that while the structural defects have decreased, the overall orderliness of the graphene lattice has not improved significantly. This phenomenon can be attributed to the introduction of MXene, which may induce a reorganization of the carbon structure in LIG.

Additionally, interfacial interactions may occur between the functional groups on the MXene surface and the carbon framework, making a more ordered carbon phase and a reduction in defects, without significantly improving the crystallinity of the layered structure. In M-MXene/LIG composite, the I_D/I_G ratio increases to 0.409, higher than that of the MXene/LIG composite, but still lower than that of pure LIG. The I_{2D}/I_G ratio is 0.631, slightly higher than that of pure LIG (Fig. S1(b) in supporting materials). This increase in the I_D/I_G ratio may be due to the introduction of additional functional groups during fluoroalkane surface modification, which causes minor structural disturbances and results in a slight rebound in defect density.

To further confirm the bonding interaction between MXene and LIG as well as the variations in surface functional groups, XPS analysis was conducted on the three materials: LIG, MXene/LIG, and M-MXene/LIG. The XPS results are presented in Fig. 2(e). The data reveal that in the pure LIG material, only typical C–C bonds and a small quantity of C–O bonds are present, indicating that its structure is predominantly composed of a porous graphitic carbon framework, which exhibits excellent conductivity and a large specific surface area. In the MXene/LIG sample, the emergence of the Ti_{2p} peak confirms the successful introduction of MXene, and the presence of C–Ti bonds suggest a certain degree of chemical bonding between MXene and LIG. For the M-MXene/LIG material, the XPS spectrum exhibited characteristic peaks corresponding to Ti–C, and Ti–O–F bonds, indicating the successful introduction of the modified components (Figs. S1(c) and S1(d) in supporting materials). Subsequently, resistance tests were conducted on strain sensors fabricated using the three different materials. As shown in Fig. 2(f), the resistance of the LIG-based sensor was measured as 35.9 Ω, while the MXene/LIG flexible wearable strain sensor exhibited a resistance of 14.1 Ω, and the M-MXene/LIG strain sensor demonstrated a resistance of 15.7 Ω.

The selected testing frequency window for this study (8 GHz–12 GHz) corresponds to typical external electromagnetic sources found in aviation and common environments. Electromagnetic shielding effectiveness (SE) is typically determined by factors such as reflection (R), absorption (A), and transmission (T) of electromagnetic waves by the material. Based on the scattering parameters measured by a vector network analyzer,

reflection coefficient

$$R = |S_{11}|^2 = |S_{22}|^2; \tag{1}$$

transmission coefficient

$$T = |S_{21}|^2 = |S_{12}|^2; \tag{2}$$

absorption coefficient

$$A = 1 - R - T. \tag{3}$$

Thus, the total shielding effectiveness can be obtained by

$$SE_T = -10\log_{10} T. \tag{4}$$

When absorption dominates ($SE_A \gtrsim 10$ dB), the total SE can be approximately decomposed as

$$SE_T \approx SE_R + SE_A, \tag{5}$$

$$SE_R = -10\log_{10}(1-R), \tag{6}$$

$$SE_A = -10\log_{10}\left(\frac{T}{1-R}\right). \tag{7}$$

As shown in Figs. 3(a)–3(f), the test results indicates that although LIG possess a three-dimensional (3D) porous structure and exhibits certain conductivity, its overall electromagnetic shielding effectiveness remains relatively low. However, when MXene is introduced into LIG to form a composite material, the electromagnetic shielding effectiveness significantly increases, reaching up to 31.5 dB (Fig. S2 in supporting materials). This improvement can be attributed to the excellent conductive properties of MXene, as its flakes exhibit metallike conductivity, which provides efficient pathways for electron migration and thereby enhance the overall electrical conductivity of the composite.

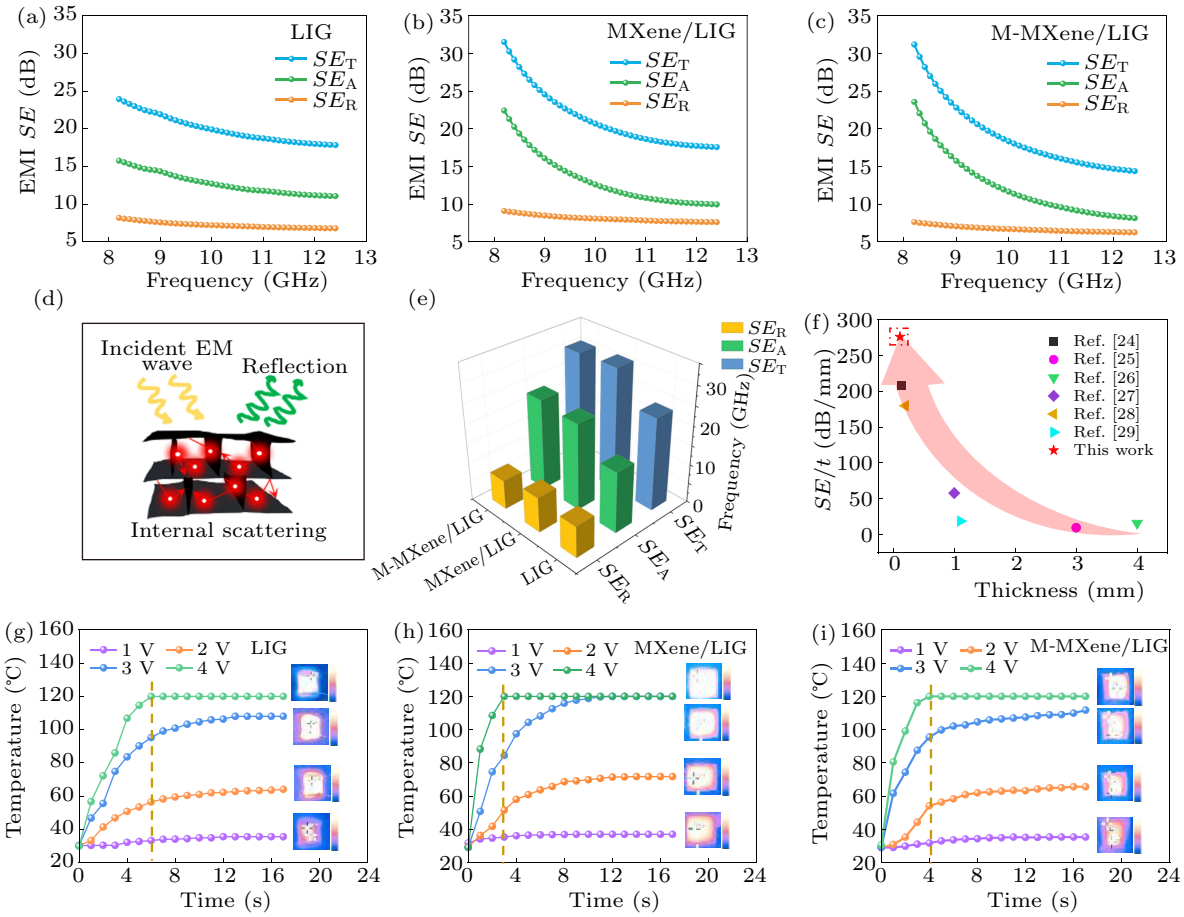


Fig. 3. Characterization of EMI shielding performance and electrothermal behavior of LIG, MXene/LIG, and M-MXene/LIG: (a) EMI test of LIG, (b) EMI test of MXene/LIG, (c) EMI test of M-MXene/LIG, (d) electromagnetic shielding mechanism diagram, (e) average values of SE_A, SE_R, and SE_T, (f) comparison chart of EMI shielding performance, (g) electrothermal performance test of LIG, (h) electrothermal performance test of MXene/LIG, (i) electrothermal performance test of M-MXene/LIG.

Furthermore, the synergistic interaction between MXene and LIG facilitates the formation of a multi-level conductive network. This structure promotes multiple reflections and absorptions of electromagnetic waves within the material, consequently enhancing its electromagnetic shielding performance. The electromagnetic shielding performance of M-MXene/LIG slightly decreases to 31.1 dB, however, it still shows a substantial improvement compared to pure LIG. The composites structure effectively maintains a multi-mechanism electromagnetic shielding performance through both reflection and absorption. Test results indicate that the incorporation of MXene effectively improves the electromagnetic shielding performance of LIG material, primarily due to the excellent metallic conductivity of MXene flakes, which, together with the 3D porous carbon framework of LIG, constructs a continuous conductive network. This leads to stronger impedance mismatch at the incident interface of electromagnetic waves, thereby enhancing the reflection effect. Simultaneously, the abundant interfaces between MXene and LIG, as well as the polar functional groups on the MXene surface, introduce interfacial polarization and dipole relaxation losses, allowing a portion of the electromagnetic wave energy to be effectively absorbed and dissipated.

Furthermore, the porous structure of LIG further extends the propagation path of electromagnetic waves within the material, promoting multiple scattering and absorption. Even after surface chemical modification of MXene, these conductive networks and interfacial polarization mechanisms are maintained, thus the overall electromagnetic shielding performance of the composite material is almost unaffected. Using ImageView software, the pore size of the MXene/LIG composite was measured to range from 5.66 μm to 15.62 μm, with an average pore size of 11.06 μm, showing a relatively uniform distribution and dense structure. In contrast, the pore size of the M-MXene/LIG composite ranged from 4.47 μm to 27.20 μm, with an average pore size of 13.86 μm, exhibiting a sparser and more uneven pore distribution. Overall, the slightly larger average pore size and higher porosity of M-MXene/LIG reduce the continuity of its conductive pathways and weaken the multiple scattering and absorption of electromagnetic waves, thereby resulting in a slightly lower overall electromagnetic shielding effectiveness. Figures 3(g)–3(i) present the heating curves (T–t) of LIG, MXene/LIG, and M-MXene/LIG under applied voltages of 1 V, 2 V, 3 V, and 4 V, respectively, with corresponding thermal images displayed on the right. Under the same voltage, all samples

exhibit a rapid temperature increase during the initial 2 s–5 s, followed by a gradual approach to a steady-state temperature. Among them, MXene/LIG demonstrates the highest heating rate and reaches thermal equilibrium in the shorter time, followed by M-MXene/LIG, whereas LIG requires the longest time to achieve a steady-state temperature. This behavior can be attributed to the mechanism of electrothermal heating governed by Joule heating. At the same voltage, the core factors determining the heating performance are the effective resistance and the thermal conduction pathway. MXene is an intrinsically highly conductive material, and the three-dimensional porous structure of LIG enables uniform bridging of MXene flakes, forming a multi-scale parallel conductive network. The significantly reduces interfacial contact resistance, thereby decreasing the overall resistance and increasing the applied power, which results in faster and more intense heating. Surface modification slightly increases the contact resistance between flakes and slightly reduces the effective conductive area to a certain extent, leading to a steady-state temperature that is marginally lower than that of the unmodified sample. Although LIG itself is conductive, its porous and discontinuous flake contact structure results in high overall resistance and lower in-plane thermal conductivity compared to the composite material, which in turn leads to slower heating and lower steady-state temperature.

3.2. Hydrophobic-sensing performance test

In the performance evaluation phase, the M-MXene/LIG-based flexible strain sensor was initially subjected to hydrophobicity analysis. As shown in Fig. 4(a), the static water contact angles of various material surfaces were measured. The untreated PI film exhibited a contact angle of approximately 56.49°, showing a distinctly hydrophilic nature. In comparisons, owing to its inherently porous and rough surface structure, LIG demonstrated a significantly increased contact angle of approximately 138.83°, reflecting pronounced hydrophobic behavior. Upon incorporating MXene into the PI film, the contact angle increased to approximately 88.53°. This improvement was attributed to the formation of a micro/nano-flake morphology on the PI surface after MXene deposition, which enhanced surface roughness. However, the MXene/LIG composite exhibited a contact angle of approximately 123.69°, which was lower than that of pure LIG. Therefore, even though MXene flakes may macroscopically increase the contact angle, their polar functional groups still increase the chemical affinity between water droplets and the surface, reducing the overall hydrophobicity. After surface chemical modification, the contact angle of M-MXene/PI increased to approximately 113.19°, whereas that of M-MXene/LIG reached approximately 151.10°, exhibiting the development of superhydrophobic properties.

Figure 4(b) illustrates the mechanism underlying the difference in surface hydrophobicity between MXene/LIG and M-MXene/LIG. The MXene/LIG relies on its micro/nano-porous structure to generate significant surface roughness, which increase the contact angle to about 123.69°, however, due to the presence of hydrophilic functional groups on its surface, it still fails to achieve superhydrophobicity. After modification with fluorine-containing groups (–CF3, –CF2), the surface free energy is significantly reduced, resulting in water droplets adopting a Cassie–Baxter state. This leads to an increase in the contact angle to approximately 151.10°, showing a typical "lotus effect." Mechanistic analysis reveals that the synergistic effect of surface roughness and low surface energy functional groups plays a critical role in achieving superhydrophobicity. This property provides long-term stable protection for flexible sensors, enabling them to maintain reliable motion signal monitoring performance in simulated flight environments. As shown in Fig. 4(c), the relationship between contact angle and surface roughness (R_a) is presented and compared with data from existing literature. Most studies indicate that the contact angle generally increases with increasing surface roughness, although the extent of this increase is typically limited. However, the M-MXene/LIG material proposed in this study exhibits not only a large surface roughness but also a contact angle exceeding 150°, significantly outperforming superior performance compared to most reference results (Fig. S3, supporting materials). This characteristic is particularly crucial for civil aviation pilot motion detection scenarios, as it enables the materials to effectively resist interference from sweat, ambient moisture, and condensation, thereby maintaining stable sensing performance.

To further investigate the sensor's long-term cyclic stability under 1% strain, figure 4(d) presents the continuous resistance variation during the stretching-releasing cycles over a period of 0 s–3600 s, corresponding to a cumulative number of cycles of approximately 1080. The resistance change curve remained stable without significant degradation, and the locally magnified waveform remained its regularity. To investigate whether the hydrophobic performance of the sensing material changes during the stretching process in cyclic loading, as shown in Fig. 4(e), the contact angle of water and sweat variation of M-MXene/LIG was measured throughout cyclic stretching. The contact angle of sweat remained between 150.2° and 148.7° within the stretching range, which was consistent with the corresponding change for the water contact angle from 151.1° to 150.0°. The results indicated that the contact angle exhibited only a minimal decrease over time, while maintaining a relatively high level, thereby preserving the sensor's protective capability in complex environments. Consequently, this flexible strain sensor demonstrates outstanding cyclic reliability and durability, making it suitable for long-term dynamic monitoring applications.

Figure 4(f) shows the relative resistance change of the flexible strain sensor under various tensile strains (1%, 2%, 3%, 4%). It can be observed that during repeated stretching

and releasing cycles, the sensor's resistance response change increasing progressively as the strain amplitude increases. This behavior indicates that the sensor can produce stable response signals under different levels of mechanical deformation, verifying its high strain sensitivity and controllable output characteristics. Subsequently, the variation in water contact angle on the M-MXene/LIG surface under different strain conditions was evaluated, as shown in Fig. 4(g). Even within the tensile strain range of 0%–4%, the contact angle of water and sweat exhibited only slight fluctuations, consistently maintaining a high value. This suggests that the surface hydrophobicity remains intact during stretching (Figs. S4 and S5, supporting materials).

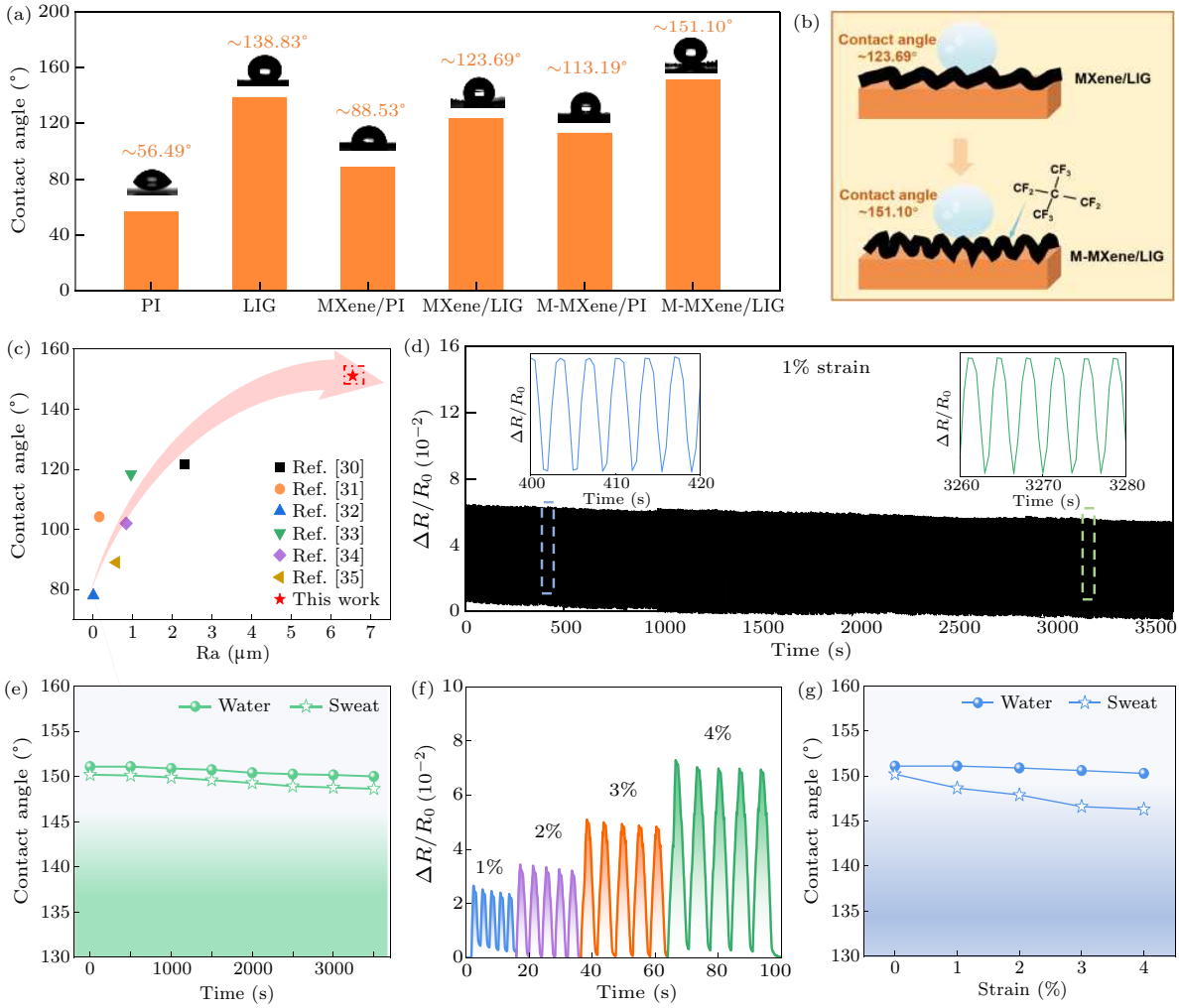


Fig. 4. Sensing performance and hydrophobicity evaluation of the flexible strain sensor: (a) water contact angle measurements on various material surfaces, (b) schematic illustration of the hydrophobicity difference between MXene/LIG and M-MXene/LIG surfaces, (c) comparative chart of hydrophobicity, (d) cyclic repeatability assessment of the flexible strain sensor, (e) water and sweat contact angle variation on the M-MXene/LIG surface during cyclic stretching, (f) relative resistance change under 1%, 2%, 3%, 4% stretch-release over five cycles, (g) water and sweat contact angle variation on the M-MXene/LIG surface at different stretch levels.

3.3. Applications of MXene/LIG-based sensors

To evaluate the application potential of the flexible multifunctional sensor in complex real-world environments, we applied it in a pilot cockpit simulation training system. Within the simulation environment, pilots are required to frequently manipulate flight control systems using their fingers and hands. Therefore, real-time monitoring of hand movements is crucial for enhancing flight safety and improving human-computer interaction. Figure 5 shows the application scenario of the flexible sensor in pilot simulator training.

The sensor was affixed to key parts of the pilot's hand, enabling the real-time acquisition of motion signals, which were then converted into measurable resistance changes without interfering with normal hand operation. Figures 5(a)–5(e) present five sets of resistance variation corresponding to distinct hand movement patterns, all of which demonstrate consistent and reproducible characteristics. Figure 5(a) illustrates the opening and closing motion between the thumb and index finger, where the sensor output curve presents obvious periodic fluctuations. Each cycle of opening and closing corresponds to a distinct resistance change, producing well-defined peaks and troughs, which indicate that the sensor can consistently distinguish subtle relative fingertip movements. Figure 5(b) shows the opening and closing movement between

the index and middle fingers. The waveform similarly displays regular fluctuations with relatively large amplitudes, indicating that this motion induces more pronounced deformation of the sensor. The high repeatability of the curve further confirms the sensor's reliability. Figure 5(c) illustrates the palm bending motion at a 90° angle, where the resistance curve displays periodic fluctuations with distinct cycles and high amplitudes, reflecting the sensor's high-sensitivity response to large-angle palm bending. Figure 5(d) shows the back-of-hand bending motion at 90°, where the waveform changes rapidly and symmetrically, indicating the sensor's prompt response to both bending and recovery processes. The significant difference between peak and trough values further suggests that the sensor is capable of accurately capturing large-amplitude bending movements. Figure 5(e) demonstrates the dorsal hand stretching-clenching motion, during which the waveform exhibits continuous periodic fluctuations with the maximum amplitude. This indicates that the motion generates the most significant strain, while the sensor signal remains stable and highly reproducible, verifying the sensor's robustness during complex dynamic movements. According to the test results, the developed flexible sensor is capable of not only monitoring subtle finger movements but also capturing large-amplitude hand bending, providing a reliable method for human-computer interaction monitoring in pilot's simulator training.

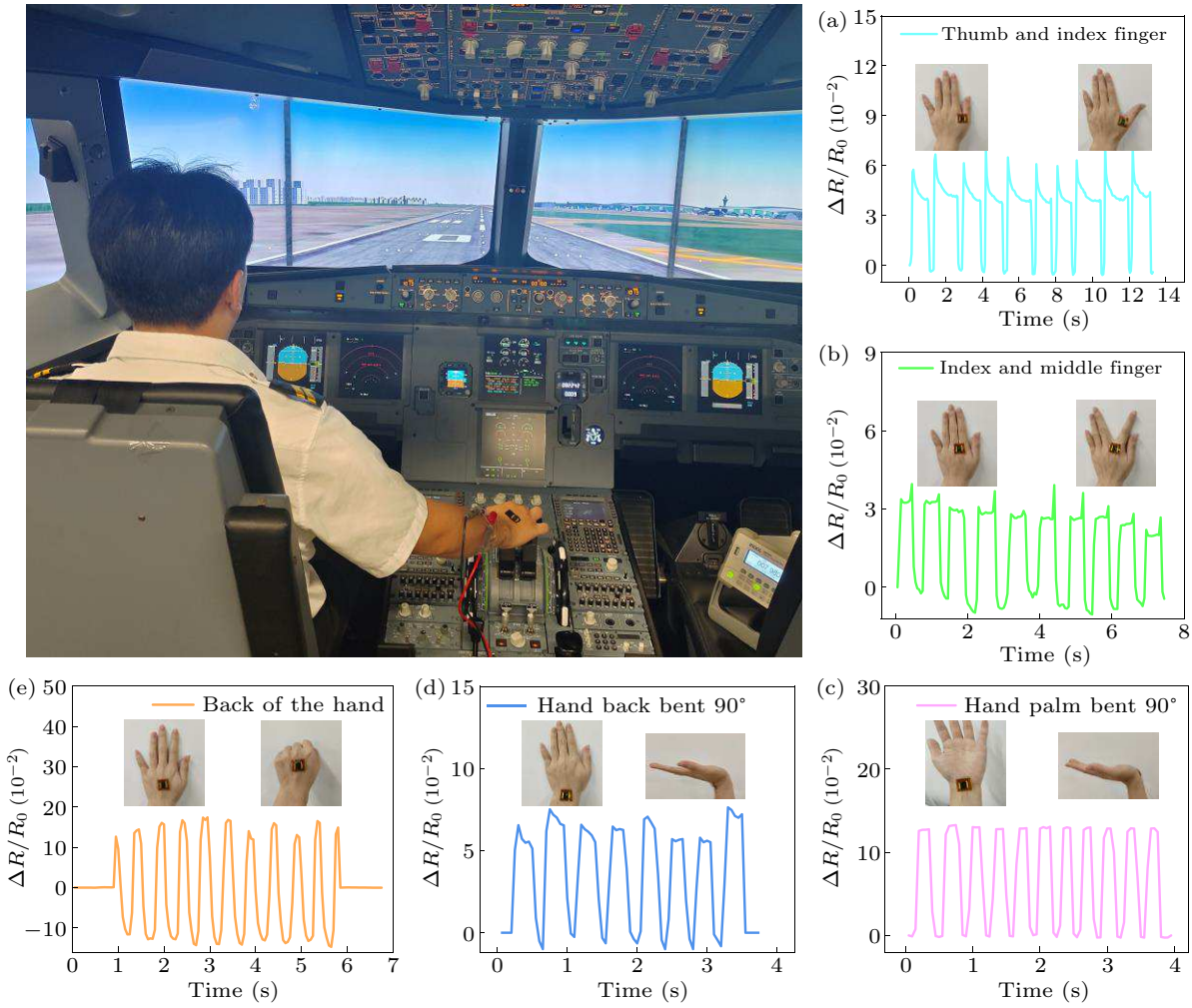


Fig. 5. Application of the flexible sensor in pilot simulator training: (a) relative resistance change during thumb-index finger abduction and adduction, (b) relative resistance change during index finger-middle finger abduction and adduction, (c) relative resistance change during 90° palm bending, (d) relative resistance change during 90° back-of-hand bending, (e) relative resistance change during extension and flexion of the dorsal hand.

4. Conclusion and perspectives

This study demonstrates the successful development of a multifunctional composite sensor based on surface-functionalized MXene and laser-induced graphene (LIG). By functionalizing MXene with CPTMS and FOTS, we effectively mitigated its intrinsic hydrophilicity and susceptibility to oxidation, thereby improving environmental stability and achieving a high hydrophobic contact angle of 151.1°. When combined with CO_2, laser direct writing technology. the sensor showed high-precision patterning capability. The resulting M-MXene/LIG composite sensor delivers exceptional multifunctional performance, including an electromagnetic shielding effectiveness of 31.5 dB, excellent hydrophobicity, precise sensing capability, and enhanced thermal conductivity. In

practical applications, such as simulated cockpit pilot training under complex environmental conditions, the sensor enables highly accurate motion capture while providing effective electromagnetic interference shielding. This work not only addresses critical challenges in multifunctional sensor design but also provides a promising pathway for advancing flexible electronics. Such technology holds significant potential for future applications in wearable devices, intelligent robotics. and human-machine interaction systems, thereby driving innovation across multiple fields.

Acknowledgements

Project supported from Research Fund on Sichuan Civil Aviation Flight Technology and Flight Safety Engineering Technology (Grant Nos. GY2024-10C and GY2025-16C), the Basic Scientific Research Expenses of Central Universities (Grant Nos. 24CAFUC03020 and 24CAFUC03022), the Graduate Research Innovation Fund of Civil Aviation Flight University of China (Grant No. 25CAFUC10018), and the Open Fund of Key Laboratory of Flight Techniques and Flight Safety, CAAC (Grant No. F2024KF24E).

References

[1] Dubey A, Ahmed A, Singh R, Singh A, Sundramoorthy A K and Arya S 2024 *International Journal of Smart and Nano Materials* **15** 2385350
[2] Ding Y F and Chen X Y 2020 *Acta Phys. Sin.* **69** 20200867 (in Chinese)
[3] Zhao G, Lv B, Wang H, Yang B, Li Z, Ren J, Gui G, Liu W, Yang S and Li L 2021 *International Journal of Smart and Nano Materials* **12** 1958085
[4] Zhang X J, Chen J X, Zheng Z H, Tang S S, Cheng B, Zhang Z W, Ma R, Chen Z T, Zhuo J T, Cao L Y, Chen Z H, He J F, Wang X F, Yang G W and Yi F 2024 *Adv. Mater.* **36** 2407859
[5] Lei X, Fan H Y, Zhao Y L, Zhong M, Wu Z H, Li L, Li S Q, Xing X X, Liu J H, Sun Y B, Jiang Y and Ren G G 2025 *Micromachines* **16** 16050513
[6] Hu Y, Wang L, Li J, *et al*. 2023 *International Journal of Smart and Nano Materials* **14** 2236997
[7] Li J J, Ji D C, Zhang Z B, Yang Y N, Zhang R C, Wang T Y, Zhang Y M, Cao W X and Zhu J Q 2024 *Chin. Phys. Lett.* **41** 038501
[8] Wang Y, Li H L, Lu S W, Liu X M, Li W, Wang X Q, Zhang L and Wang Q X 2023 *International Journal of Smart and Nano Materials* **14** 2184880
[9] Xie Y D, Lu M Y, Yin W L, Xu H Y, Zhu S, Tang J W, Chen L M, Ren Q Y, Zhang Y N and Qu Z G 2019 *IEEE Sensors Journal* **20** 2943487
[10] Liu Y C Y, Li X F, Yang H L, Zhang P, Wang P H, Sun Y, Yang F Z, Liu W Y, Li Y J, Tian Y, Qian S, Chen S D, Cheng H Y and Wang X F 2023 *ACS Nano* **17** 11267
[11] Yang S Y, Yang W K, Yin R, Liu H, Sun H L, Pan C F, Liu C T and Shen C Y 2023 *Chemical Engineering Journal* **453** 139716
[12] Zhong M, Li S C, Zou Y, Fan H Y, Jiang Y, Chao Q, Luo J L and Yang L 2024 *Micromachines* **15** 15020285
[13] Zou Y, Zhong M, Li S C, Qing Z H, Xing X Q, Gong G C, Yan R, Qin W F, Shen J Q, Zhang H Z, Jiang Y, Wang Z H and Zhou C 2023 *Polymers* **15** 15173553
[14] He Q, Liu Y J, Xu Z H, Wang J W, Jia Y Y, Wang G F ang Li A L 2025 *Materials Today Chemistry* **47** 102824
[15] Wang H, Zhao Z F, Liu P P and Guo X G 2022 *Biosensors* **12** 12020055
[16] Weng C X, Xing T L, Jin H, Wang G R, Dai Z H, Pei Y M, Liu L Q and Zhang Z 2020 *Composites Part A: Applied Science and Manufacturing* **135** 105927
[17] Lian X J, Fu J K, Gao Z X, Gu S P and Wang L 2023 *Chin. Phys. B* **32** 017304
[18] Aakyiir M, Yu H, Araby S, Wang L Y, Michelmore A, Meng Q S, Losic D, Choudhury N R and Ma J 2020 *Chemical Engineering Journal* **397** 125439
[19] Deng C H, Zhao S Q, Su E M, Li Y T and Wu F M 2021 *Advanced Materials Technologies* **6** 2100574
[20] Kumar S, Mehdi S M Z, Taunk M, Kumar S, Aherwar A, Singh S and Singh T 2025 *J. Mater. Chem. A* **13** 11050
[21] Mozafari M and Soroush M 2021 *Materials Advances* **2** 7277
[22] Yang W, Liu J J, Wang L L, Wang W, Yuen A C Y, Peng S H, Yu B, Lu H D, Yeoh G H and Wang C H 2020 *Composites Part B: Engineering* **188** 107875
[23] Luo J C, Gao S J, Luo H, Wang L, Huang X W, Guo Z, Lai X J, Lin L W, Robert K Y L and Gao J F 2021 *Chemical Engineering Journal* **406** 126898
[24] Chu N, Luo C J, Chen X S, Li L X, Liang C B, Chao M and Yan L K 2023 *J. Alloys Compd.* **955** 170241
[25] Lin T F, Yu H J, Wang Y, Wang L, Vatsadze S Z, Liu X W, Huang Z K, Ren S N, Uddin M A, Amin B U and Fahad S 2021 *J. Mater. Sci.* **56** 18093
[26] Yang S D, Yang R L, Lin Z Q, Wang X M, Liu S J, Huang W B, Chen Z B, Wei J H, Zeng Z P, Chen H J, Hu Y G and Gui X C 2022 *J. Mater. Chem. A* **10** 23570
[27] He P, Wang X X, Cai Y Z, Shu J C, Zhao Q L, Yuan J and Cao M S 2019 *Nanoscale* **11** 6080
[28] Anand S and Pauline S 2021 *Advanced Materials Interfaces* **8** 2001810
[29] Kumar R, Macedo W C, Singh R K, Tiwari V S, Constantino C J L, Matsuda A and Monshkalev S A 2019 *ACS Applied Nano Materials* **2** 4626
[30] Alva P G, Lizarraga K K G, Parra R G, Barba A, Banuelos J G and Hernandez M 2025 *Surface and Interface Analysis* **57** 7420
[31] Al-Radha, BDS, MSc, *et al*. 2016 *OSR Journal of Dental and Medical Sciences* **15** 2279
[32] Ji W Y, Liu M, Li Y P, Liu L L, Wang Y H, Duan F, Su C L, Li H B, Cao R Q, Yin J Y, Wei M J, Jiang Z Y and Cao H B 2024 *Small* **20** 2405113
[33] Razavifar M, Abdi A, Nikooee E, Aghili O A and Riazi M 2025 *Sci. Rep.* **15** 16611
[34] Chen Y R, Xia W C and Xie G Y 2018 *Fuel* **222** 140
[35] Alnoush W, Sayed A, Solling T and Alyafei N 2021 *Journal of Petroleum Science and Engineering* **203** 108679